Author Manuscript

Optimizing MRF-ASL Scan Design for Precise Quantification of Brain Hemodynamics using Neural Network Regression

Anish Lahiri[1], Jeffrey A Fessler[1], and Luis Hernandez-Garcia[2]

[1]Department of Electrical and Computer Engineering, University of Michigan
[2]Functional MRI Laboratory, University of Michigan

Corresponding Author: Anish Lahiri
Address: Functional MRI Laboratory, 2360 Bonisteel Blvd, Ann Arbor, MI 48105, USA.
E-mail: anishl@umich.edu
Word count: 4808
Running Title: Optimizing ASL Fingerprint Acquisition

1

Abstract

Purpose: Arterial Spin Labeling (ASL) is a quantitative, non-invasive alternative for perfusion imaging that does not use contrast agents. The magnetic resonance fingerprinting (MRF) framework can be adapted to ASL to estimate multiple physiological parameters simultaneously. In this work, we introduce an optimization scheme to increase the sensitivity of the ASL fingerprint. We also propose a regression based estimation framework for MRF-ASL.

Methods: To improve the sensitivity of MRF-ASL signals to underlying parameters, we optimized ASL labeling durations using the Cramer-Rao Lower Bound (CRLB). This paper also proposes a neural network regression based estimation framework trained using noisy synthetic signals generated from our ASL signal model. We tested our methods in silico and in vivo, and compared with multiple post labeling delay (multi-PLD) ASL and unoptimized MRF-ASL. We present comparisons of estimated maps for the six parameters of our signal model.

Results: The scan design process facilitated precise estimates of multiple hemodynamic parameters and tissue properties from a single scan, in regions of normal gray and white matter, as well as regions with anomalous perfusion activity in the brain. In particular, there was a 86.7 % correlation of perfusion estimates with the ground truth *in silico*, using our proposed techniques. *In vivo*, there was roughly a 7 fold improvement in the Coefficient of Variation (CoV) for white matter perfusion, and 2 fold improvement in gray matter perfusion CoV in comparison to a reference Multi PLD method. The regression based estimation approach provided perfusion estimates rapidly, with estimation times of around 1s per map.

Conclusions: Scan design optimization, coupled with regression-based estimation is a powerful tool for improving precision in MRF-ASL.

Keywords: Arterial Spin Labeling, Magnetic Resonance Fingerprinting, Optimization, Cramer-Rao Bound, Scan Design, Regression, Neural Networks, Deep Learning, Precision, Estimation, Brain Hemodynamics.

1   Introduction

Quantitative imaging of tissue properties is gaining increasing prominence in the diagnosis, prognosis and treatment planning of several diseases, e.g., [14, 21, 33, 31]. Moving beyond the variations associated with qualitative intensity-based imaging allows gleaning information focused on the physiological phenomena being investigated. In the context of cerebrovascular disorders, quantitative perfusion imaging has found several applications [12, 19, 38, 10, 17, 3, 16, 9, 2]. Typically, quantitative imaging of perfusion involves gadolinium-based contrast enhanced MRI, which suffers from lack of fast repeatability and risks involved in cases of subjects with nephrogenic disorders [37, 32].

Arterial Spin Labeling (ASL) [11] provides an alternative to contrast agent based MRI by magnetically labeling blood flowing into organs or tissues of interest. ASL temporary inversion of the spins present in flowing blood upstream of the organ under scrutiny, by applying radiofrequency (RF) magnetic pulses. These inverted spins then behave like an *endogenous* tracer that is detectable after it perfuses into the tissue in the relevant organ shortly afterwards. ASL is non-invasive, non-toxic, quickly repeatable and has a much simpler workflow than contrast enhanced MRI. However, ASL images are limited by low spatial and temporal signal-to-noise ratio (SNR) [30, 39, 7]. This drawback is more pronounced in white matter, where traditional ASL methods perform poorly[36]. Estimating perfusion using ASL requires knowledge of a number of tissue properties or hemodynamic factors that are usually fixed to literature values. In reality, some of these (tissue T_1 for example) vary significantly from region to region. Fixing these parameter values can lead to significant biases in perfusion estimates and efforts to estimate such factors from separate scans can be undesirably time-consuming.

2

MRF is a recently developed technique [24] that estimates multiple hemodynamic parameters and tissue properties simultaneously from a single acquisition. This approach improves accuracy at the possible expense of precision in estimates. Nevertheless, information accrued from the additional estimated parameter maps may aid understanding of physiological conditions. MRF utilizes transient signals obtained by varying imaging parameters such as the repetition time (TR) or flip angles as identifiers for the underlying physiological factors. A standard approach to multiparametric estimation using such a technique involves searching through 'dictionaries' consisting of signals generated by feasible combinations of parameters, in a Maximum Likelihood manner. In an ASL based fingerprinting [35, 41] setting, the observed signal depends on several parameters (typically 5-7), presenting a considerable challenge to precise estimation. For example, with more parameters to estimate, it becomes difficult to maintain and search a 'fine' dictionary. Specifically, [35] reports a 2 hr estimation time for a single slice, with a dictionary quantization of 6mL/100g/min for perfusion.

As an alternative, this paper uses a regression-based estimator to generate predictions from fingerprint data. While the use of regressors for MRF-based estimation has become more prevalent recently [27, 8], our preliminary work [20] was the first to investigate neural network regression for ASL Fingerprinting, where there are considerably more parameters to estimate. Estimation using neural network regression allows for much faster estimation, and overcomes quantization error.

Regardless of the estimation technique used, if the ASL fingerprints themselves are insufficiently sensitive to the underlying parameters, then estimates obtained from them will lack precision. Thus, the first goal of this paper is to increase the information conveyed by fingerprints. This is done using Cramer-Rao bound based optimization of scan parameters in ASL. An example of such scan parameters are the labeling durations in the scan. While there has been some work on optimizing scan-design for MR sequences in quantitative imaging [26, 43], and even specifically in ASL [42, 40], our work is the first to investigate it in an ASL fingerprint setting. While most other pertinent methods focused on providing precise results in regions of gray matter, we use a cost function having a comprehensive uniform prior. This enables precise estimation over a wide range of feasible parameter values, including white matter or potential anomalies. We also constrain our optimization procedure to adhere to a fixed scan time for practicality. The primary focus of our work is to establish the need for scan design optimization regardless of the estimation technique involved. Through our work, we establish that optimized scan design coupled with regression-based estimation should further the transition of ASL Fingerprinting to clinical use.

The rest of the paper is organized as follows: Section 2 introduces the ASL signal model used in this work. This model, along with a Cramer-Rao bound based cost function, is used to optimize our scan design. Next, we design a neural network regressor for estimating hemodynamic parameters and tissue properties. The neural network is trained using fingerprints simulated with a combination of the optimized scan design and the described model. We also devise a post-processing technique to mitigate nuisance effects in our acquisitions. Thereafter, we describe the creation of in-silico datasets to test the performance of our methods, as well the methods we compare to in our work. We then describe the in-vivo experiments we performed in the validation of our designed methods. Section 3 shows the theoretical predictions of the performance of our scan design, as well as the results of comparisons in-silico and in-vivo with other methods, namely two other MRF ASL scans found in literature and multi-PLD ASL. Section 4 elaborates upon these results and the inferences we draw from them. Section 5 describes our conclusions.

3

2 Methods

2.1 ASL Signal Model

To describe the ASL signal in the brain for scan design optimization and parameter estimation, we used the two-compartment model depicted in Fig. 1. Although the single compartment model introduced in [5] has been the *de-facto* standard in ASL literature in the past, several works [29, 44, 4, 6, 28] have raised issues of oversimplification associated with single-compartment modeling, and have adopted two-compartment models. For ASL fingerprinting, such models have been highlighted in [41, 34]. Our chosen model for the ASL signal consisted of separate compartments for blood in tissue and arteries, as well as an additional compartment to incorporate Magnetization Transfer effects. In the model, magnetically labelled blood flows into the arterial compartment through the arterioles, and perfuses into the tissue compartment therein. The Cerebral Blood Volume fraction (CBVa) determines the portion of the acquired signal to which each compartment contributes, and T_1 relaxation of blood and tissue is accounted for in the signal description. The longitudinal magnetization of the tissue compartment thus evolved as:

$$\frac{dM_{\text{tis}}(t)}{dt} = -\frac{M_{\text{tis}}^0 - M_{\text{tis}}(t)}{T_{1,\text{tis}}} + f \cdot M_{\text{art}}(t) - \frac{f}{\lambda} \cdot M_{\text{tis}}(t) - K_m(t) \cdot M_{\text{tis}}(t), \tag{1}$$

where M_{tis} and M_{art} represent the magnetization in the tissue-compartment and the arterial compartment respectively, λ is the blood-brain partition coefficient, K_m is the Magnetization Transfer rate (MTR), f is the rate of perfusion. Here, $T_{1,\text{art}}$ is the arterial relaxation time, and $T_{1,\text{tis}}$ (truncated to T_1 in later sections) the relaxation time of tissue. The input to the arterial compartment was determined by a labeling function, that is described in eqn. (2). The arterial magnetization was described using an input or labeling function as follows:

$$M_{\text{art}}(t) = 1 - 2 \cdot \alpha \cdot \text{inp}(t) \cdot e^{-\frac{(t-\delta)}{T_{1,\text{art}}}}, \tag{2}$$

where α is the inversion efficiency, δ is the Bolus Arrival Time (BAT), and

$$\text{inp}(t) = \begin{cases} 1, & \text{for labeling pulses} \\ 0, & \text{otherwise.} \end{cases}$$

The total longitudinal magnetization was thus described as:

$$M(t) = CBV_a \cdot M_{\text{art}} + (1 - CBV_a) \cdot M_{\text{tis}}, \tag{3}$$

where CBV_a is the Cerebral Blood Volume fraction described earlier. The observed ASL-MRF signal, $M(t) \cdot \sin(\beta)$, where β is the flip angle, was sampled at the time(s) of acquisition, which were dictated by the scan schedule. We used signals generated using this model for both optimization of scan design as well as for training the neural network estimators. For the purposes of our work, the values of λ and α were set to 0.9 and 85% respectively.
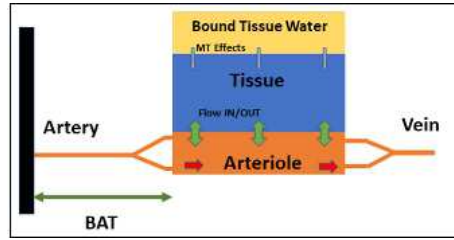
4

Figure 1: Two compartment ASL signal model used for both optimization and estimation. The unknowns in the model were: perfusion from the arteriole to the tissue, arrival time of the labeled blood bolus at the arteriole, the magnetization transfer rate, the arterial blood volume fraction, and the relaxation time of water in tissue.

2.2 Pulse Sequence

In ASL Fingerprinting, each repetition time (TR) in the sequence consists of a labeling period (T_{tag}), post labeling delay (T_{delay}), followed by a small period for signal acquisition (T_{aq}), (ideally instantaneous, but usually accounted for) and a period for adjustment (T_{adjust}) before the next label/control occurs. Every pulse in the sequence can either be a label, control, or 'silence' (where there is no RF excitation at all). In this work, we vary the TR by changing the labeling durations, while holding all other parameters of the pulse sequence fixed ($T_{\text{delay}} = 55$ms, $T_{\text{aq}} = 32.4$ms, $T_{\text{adjust}} = 50$ms). The TRs in our sequence were varied to generate a signal that is informative of the underlying parameters. Section 2.3 describes how we optimized the aforementioned labeling durations by picking from a set of candidate schedules. The label-control order (also referred to as the 'label order' later) was pseudo-randomized, but had approximately equal numbers of label, control and silence pulses. We ensured that the total duration of the scan was fixed regardless of the number of pulses, or the duration of individual TRs. This fixed total duration was discretionary. Here, we acquired 700 images for our fingerprint, with a total scan duration of 600s for a single slice.

2.3 Optimization with CRLB

A major focus of our work was to investigate the benefits of scan design optimization in ASL Fingerprinting. From an information theoretic standpoint, the total information present in a signal about the underlying parameters that generated it is independent of the estimator used to quantify the parameters themselves. For example, in a regression-based estimation framework, if the signals (or 'fingerprints') themselves are too correlated, corresponding estimates will be imprecise. This is regardless of whether kernel methods or neural networks are used. In an effort to make our fingerprints more informative or sensitive to parameters like perfusion or BAT, we used the Cramer-Rao Lower Bound (CRLB) to optimize the scan design parameters (namely, the labeling durations).

The CRLB represents the minimum variance in estimates that any unbiased estimator can achieve, for a particular signal model and noise level. We focused on magnitude image data and modeled the noise as real additive white Gaussian noise (AWGN) with standard deviation σ (empirically calculated to be 0.01, which was low enough to justify the assumption of Gaussian noise in regions with sufficient SNR). Our signal model was $\underline{s}(\underline{\theta}; \underline{\nu}) : (\mathbb{R}^p \times \mathbb{R}^l) \to \mathbb{R}^t$, where $\underline{\theta} \in \mathbb{R}^p$ represents the p hemodynamic parameters of interest, and $\underline{\nu} \in \mathbb{R}^l$ are the l scan parameters for a scan with t time points. The CRLB is expressed as the inverse of the Fisher Information matrix. Fisher Information describes the amount of information conveyed by an observable random variable about the parameters that generated it. It can be considered to be a measure of

5

sensitivity of a signal to underlying parameters and is expressed as the $p \times p$ matrix:

$$\mathbf{F}(\underline{\theta}; \underline{\nu}) = \frac{1}{\sigma^2} \cdot [\nabla_{\underline{\theta}} \underline{\mathbf{s}}(\underline{\theta}; \underline{\nu})]^T [\nabla_{\underline{\theta}} \underline{\mathbf{s}}(\underline{\theta}; \underline{\nu})], \tag{4}$$

where we calculated the signal gradient matrix, $\nabla_{\underline{\theta}} \underline{\mathbf{s}}(\underline{\theta}; \underline{\nu}) \in \mathbb{R}^{t \times p}$ numerically at each time point using Newton's central difference method[1]. To design a 'good' fingerprinting sequence, we optimized over a set of feasible scan design parameters $\underline{\nu} \in \mathcal{V}$, which in our case were the labeling durations. In our optimization, we minimized our design cost function at a representative collection or set of true parameter values, Θ. These values were spread uniformly over a range. We picked our 'optimized' labeling schedule as the one that, among all others in the feasible set $\mathcal{V}$, minimized the following cost function:

$$\hat{\underline{\nu}} = \underset{\underline{\nu} \in \mathcal{V}}{\arg \min} \ \frac{1}{|\Theta|} \sum_{\underline{\theta} \in \Theta} \text{Tr}\left(\boldsymbol{W} \cdot \left(|\boldsymbol{F}^{-1}(\underline{\theta}, \nu)|^{0.5} \oslash \boldsymbol{N}(\underline{\theta}) \right) \cdot \boldsymbol{W} \right), \tag{5}$$

where $\oslash$ denotes Hadamard division, $\boldsymbol{W}$ is a diagonal weighting matrix assigning priority to each hemodynamic parameter in the cost function, $|\Theta|$ denotes the number of points at which the normalized standard deviation is evaluated in the cost, and $\boldsymbol{N}(\underline{\theta}) = (\underline{\theta}^{0.5})(\underline{\theta}^{0.5})^T$ is a normalization matrix that is divided element-wise into the inverse Fisher Information matrix.

We used exhaustive search to minimize the design cost function (5) to ensure that our optimized scan yields precise estimates over the set Θ of 'ground truth' parameter values. Minimizing the above expression is tantamount to minimizing the average normalized standard deviation of parameter estimates, weighted appropriately, over a set of ground truth parameter values. Using normalized standard deviation bypasses having to combine variances of different values and units, and emphasizes cases when the standard deviation is comparable to the ground truth parameter value. For our experiments, we assigned twice the weight to perfusion precision as to all the other parameters in the cost function, which were weighted equally. The cost was evaluated numerically. For the optimized scheme to function well even at values seen in pathological conditions, we used an adequately large feasible range for Θ. Specifically, the parameter ranges we used were: 12-90 ml/100g/min for perfusion, 0.002-0.03 for CBVa, 0.36-1.7 s for BAT, 0.01-0.03 s^{-1} for MTR, 0.3-3.3 s for T_1 and 54-112 degrees for flip angles. $|\Theta|$ was picked to be 50 during labeling schedule optimization, and 75 during label order optimization and 250 for final evaluation of the designed scan. These points were picked using a uniform random distribution on the range for Θ described earlier. $|\Theta|$ was set to a lower number during optimization because increased number of parameter space evaluations would increase optimization time. We chose a uniform random distribution for the points to capture a wide variety of anomalous behaviour.

The set of feasible candidate labeling schedules, $\mathcal{V}$, consisted of ASL timing sequences with variable labeling times but fixed pre and post labeling delays. Thus, TR was allowed to vary depending on the labeling duration. As shown in Fig. 2, each labeling schedule (essentially a collection of labeling durations) in this set was described using a linear interpolation between 5 points in the 'labeling space'. These points were spaced at a regular number of frame intervals (here, 175). Candidate schedules were created in a 'connect-the-dots' fashion from the resulting grid of points in the labeling space, as depicted in Fig. 2. The total number of feasible schedules in this case is 11^5. We chose linear interpolation as it allowed us to explore this labeling space effectively. It also allows for flexible finer sampling of the labeling space upon increasing the number of interpolation points or possible labeling durations. Albeit, this refinement would require more optimization time. Feasible schedules were scaled to be a fixed total duration (or scan duration), before the

---

[1] $\nabla_{\underline{\theta}} \underline{\mathbf{s}}(\theta; \underline{\nu}) = \frac{\underline{\mathbf{s}}(\theta+h) - \underline{\mathbf{s}}(\theta-h)}{2h} \in \mathbb{R}^t$ for a single parameter θ
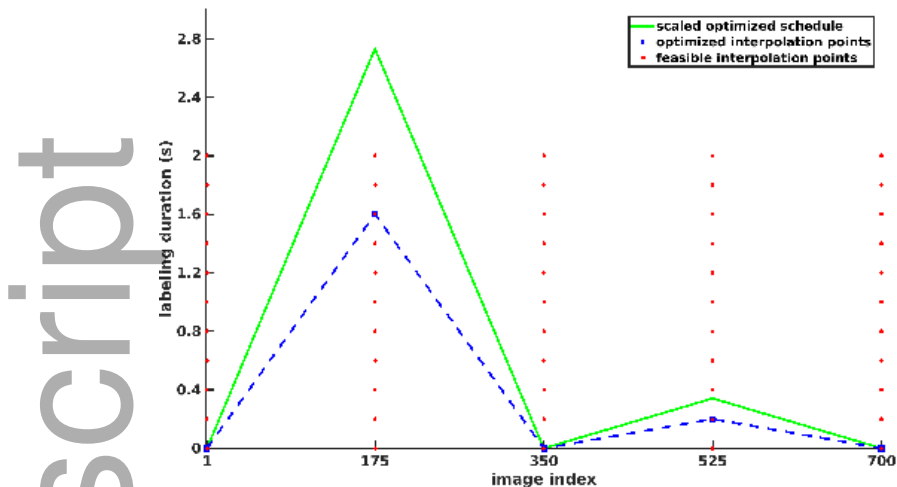
6

Figure 2: The red dots depict the feasible points for interpolating between or exploring the labeling space. The blue squares depict the label durations for the five interpolation points that, once scaled, leads to our optimized schedule. The green line depicts this scaled, best (among other candidates) schedule.

cost function was evaluated. Because there is a trade-off between sacrificing scan duration and sacrificing precision, the total duration may vary based upon the required precision. For our work, the scan duration is set to 600s. Acquiring a small number of images for this total scan duration would create labeling schedules with unreasonably long tagging times, while acquiring a large number of images increases memory and storage overhead. Under these considerations, we choose to acquire 700 images. Fig. 2 also depicts the optimized scan. Having obtained an optimized labeling schedule, we further minimized the predicted precision of flow estimates by trying several pseudo-random label-control-silence schedules while maintaining that the number of each are equal in our schedules. In section 3.1, we compare the theoretical performance of this labeling schedule to two others commonly encountered in MRF literature, with $|\Theta|$ set to 250. While the neural network-based estimation framework described in section 2.4 may provide biased estimates, these CRLB predictions serve as a useful indicator for the performance of a schedule in terms of precision in estimates obtained from it. We also note that given the non-convexity of the optimization space, and our use of discrete search in solving the problem, the resulting scan cannot be dubbed 'optimal'. However, it should perform better than the other evaluated candidates. Because it is the result of our optimization, we call the output 'optimized' ASL-MRF scan.

2.4 Estimation with Neural Networks

We used a neural network based framework to estimate 5 hemodynamic properties of relevance in our model. Namely, these were the Perfusion f (CBF), the Bolus Arrival Time (BAT) or δ, the Cerebral Blood Volume in artery (CBVa), Magnetization Transfer Rate (K), and the tissue relaxation time, henceforth called T_1 for simplicity. Additionally, we also estimated a field map of the Flip angles enacted by the scanner. Separate neural networks were used in the estimation of each parameter. The reason for moving away from the combined neural network framework used in our previous work [20] is to avoid the need for the relative weighting of targets during network training. Table 1 provides the architectural specifications of the networks used. The neural networks were chosen from a small set of candidate networks. When choosing, the

7

performance of these was tested using three validation datasets similar to the simulated phantom described in section 2.6.1, but with different ground truth values. Some of the networks required fewer nodes/layers than the others. This may be because of the varying degree of non-linear dependence of the fingerprints on different parameters.

Parameter	Depth	Architecture (nodes per layer)	min value	max value
Perfusion	3	10-10-10	0 mL/100g/min	90 mL/100g/min
CBVa	3	10-10-10	0	0.015
BAT	2	10-5	0.3 s	3.0 s
MTR	4	10-10-5-5	0 s^{-1}	0.03 s^{-1}
T_1	1	20	0.33 s	3.33 s
Flip	1	20	48°	112°

Table 1: Description of the neural network architectures used in estimating hemodynamic parameters in our signal model, as well as the respective maximum and minimum values of the ranges used in the training data. The 'Architecture' column provides the number of nodes in every layer, separated by hyphens, starting from the input. Each node in the network learns a weight and a bias during training. The input to the networks are fingerprints generated from our designed optimized sequence, which has 700 frames.

To train our networks, we used 6×10^6 samples of synthetic fingerprints generated from the model described in section 2.1, with added real white Gaussian noise with standard deviation 0.01, along with the corresponding generating parameters (Fig. 3). The same training dataset was used across all neural networks. We used an independent uniform prior on values of each parameter for generating this data. The associated parameter ranges are also depicted in Table 1. We selected the ground truth parameter values for training signals from independent uniform distributions. We did this in hopes that the trained network can perform well at estimating possible anomalies in combinations of hemodynamic properties. (For example, elevated arterial transit time, but normative perfusion etc.) Each signal was normalized by the value of the first frame in the fingerprint. We applied the same process to signals obtained from the scanner, thereby ensuring consistency during testing and training. The cost function used to train the neural networks was Mean Square Error, the optimizer associated was ADAM [18], and the non-linearities were implemented as ReLU-s. Training times for the networks were roughly $15-20$ mins. Once trained, the network was tested on a gamut of test datasets described in section 3.
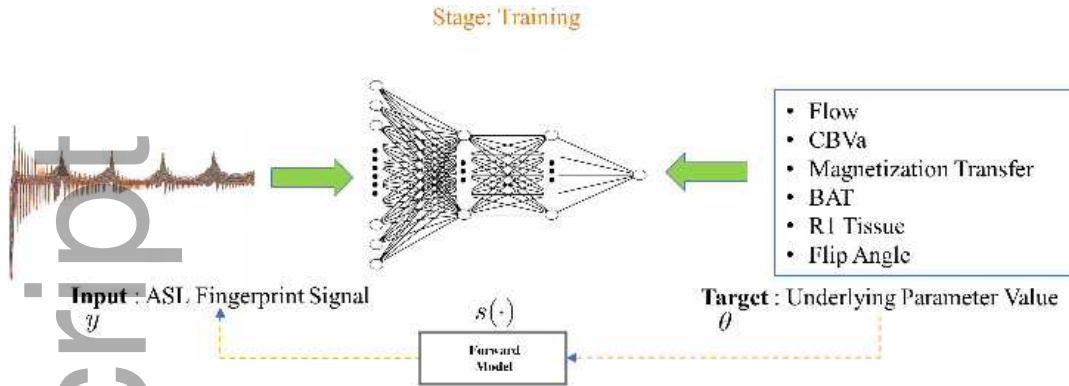
8

Figure 3: Diagram depicts a neural network regressor used as an estimator in our work, in the training stage. The targets for the training and the inputs are related through the forward model depicted in Fig. 1 with additive noise. Separate networks are trained for the different unknowns in the model. Once trained, the estimators can predict the generating parameters for a new fingerprint.

For training, we used simulated noisy fingerprints from the signal model instead of real fingerprints for two reasons: (i) ground truth estimates for real data are difficult to obtain. In a wide-scale multiparametric setting such as ours, they would suffer from granularity owing to the use of dictionary based methods in calculating the ground truth for training. They may also be biased because they were obtained from non-MRF techniques (ii) limited availability of real training data would pose a significant risk of overfitting neural networks (especially deeper ones).

2.5 Signal Preconditioning

Presence of scanner drift or cardio noise and breathing can cause severe distortions in the fingerprints from the hypothesized model [23, 15]. However, the labeling scheme modulates the perfusion information into the high frequency bands of the fingerprint signal similar to [22, 25]. This property, combined with the fact that the aforementioned nuisances generally manifest as low frequency components, motivated us to high-pass filter the fingerprints (both during training and testing) of the neural networks associated with perfusion, bolus arrival time, magnetization transfer rate and the cerebral blood volume fraction. We applied a 4-th order Butterworth filter with a cutoff at 0.05 Hz (when assuming the fingerprint was sampled at 1 Hz) for this purpose.

2.6 Data Collection

2.6.1 Simulated Anthropomorphic Pathological Phantoms

We synthesized a set of test data from hemodynamic parameter maps that closely reflected the corresponding spatial distributions in a digital phantom generated from standard gray and white matter maps (SPM12) [13]. We then introduced regions of abnormally elevated and reduced perfusion to it to quantify the performance of our methods on a range of normative and pathological parameter values. Real AWGN with standard deviation 0.01 was added to the fingerprints after generation. When estimating perfusion, CBVa, and BATs, the data was high-pass filtered as explained in section 2.5. Fig. 4 compares the predictions with the corresponding ground truths.
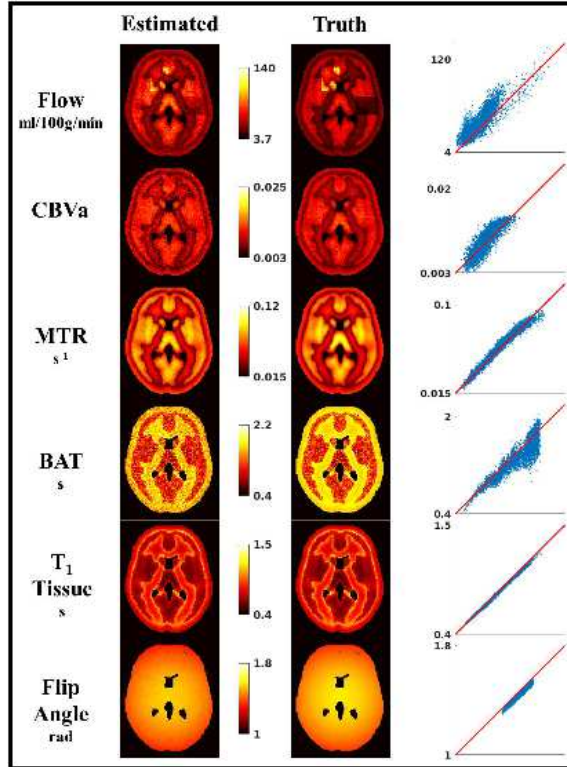
9

Figure 4: Performance of proposed neural network based estimation on the simulated dataset described in section 2.6.1. The first column depicts the predictions from the networks, while the second shows the corresponding ground truth parameter images. The third column are 'truth-vs-predicted' scatter plots of the former columns.

2.6.2 In vivo experiments

In-vivo data was acquired on a 3T General Electric MR750 scanner. The imaging parameters were: a single slice placed above the ventricles, single shot spiral readout, nominal resolution = $3.5 \times 3.5 \times 7$ mm^3, matrix size = 64×64, bandwidth = 125 Hz and TE = 5ms, FOV = 240 mm. We tested our methods on data acquired from six human subjects. For four of these subjects, we also acquired data with two other MRF-ASL scan designs (similar to the ones used in [35, 41] and described in more detail later). We compared our optimized scan design to them using similar estimation techniques (same neural network architecture and training target distribution in Table 1). Our goal was to show the benefits of labeling sequence optimization in ASL fingerprinting. For 'random scan', we sampled the labeling durations from a uniform random distribution, while in 'decreasing affine scan', the durations decrease linearly with the image index. Both schemes were designed to be 700 frames and 600s long, and are collectively described as reference ASL-MRF scans later in this text. The metric for this comparison was the normalized standard deviation of parameter estimates obtained from the numerical CRLB evaluation described in section 2.3.

For all six subjects, we also performed a 409s multi-PLD ASL [40, 1] experiment with 40 PLDs, involving a single average over label-control pairs at each PLD. The post-labeling delays were chosen according to the protocol presented in [40]. No arterial suppression was used. The CBF, CBVa, BAT and T_1

10

maps obtained from these were compared to those from our methods. We fit the signals to a single compartment model in order to obtain CBF, BAT and T1. For fair comparison, we also fit these signals to a two-compartment model to account for the arterial signal and also estimate CBVa, as in the proposed MRF method.

We used a two-stage estimation technique to generate quantitative parameter maps from the multi-PLD data. In the first stage, we estimated the tissue T_1 and M0 maps at every voxel by applying a least squares fit using the model in eqn. 1. For this stage, all other parameters in the equation were fixed to nominal, or where applicable, normative values. Next, the entire process was repeated for estimating the CBF, CBVa and BAT at each voxel (only CBF and BAT for single compartment estimation), but using M0 and T_1 values obtained in the previous stage. The MTR and flip angles were held fixed throughout.

3 Results

3.1 Optimized Scan Design

We compared the predicted performance of our optimized scan design against two reference ASL MRF scan designs described in section 2.6.2. Table 2 lists the predicted normalized standard deviation in estimates of each parameter for all three labeling schemes, and the total weighted design cost associated with each scheme. Of the 11^5 schedules evaluated, 371 were within 3% of the total cost. Of these, 150 schedules followed a similar pattern to the schedule with the minimum cost. While the other scans within the 3% margin were very different from the minimum-cost scan, these could also be grouped to be similar to $\approx 4-5$ different scan designs.

Parameter	normalized std deviation (%)		
	optimized scan	random scan	decreasing affine scan
Perfusion	46.4	51.0	46.1
CBVa	17.2	21.9	19.5
BAT	1.3	2.1	1.6
MTR	121.1	124.2	137.1
T_1	0.6	0.4	1.1
Flip	0.4	0.2	0.8
Cost	**233.4**	**250.8**	**252.3**

Table 2: Predicted normalized standard deviation of parameter estimates (in %) for ASL-MRF labeling schedules used in our comparisons. The last row shows the overall weighted design cost associated with each scheme based on eqn. (5).

3.2 Simulated Anthropomorphic Pathological Phantoms

Fig. 4 depicts the estimated maps from the Anthropomorphic Pathological phantom simulation, and the corresponding ground truth parameter images in the first two columns. From these images, we also generated 'truth vs predicted' scatter plots for each estimated parameter map to better visualize the accuracy and precision of our methods, shown in the third column of Fig. 4. For a more quantitative evaluation of the performance of our methods, Table 3 shows the correlations between the voxel values of the truth and estimated

11

parameter maps, across multiple scan designs. The corresponding root mean squared errors (RMSEs) are provided as well.

Parameter	optimized scan		random scan		decreasing affine scan	
	Corr. (%)	RMSE	Corr. (%)	RMSE	Corr. (%)	RMSE
Perfusion (ml/100g/min)	**86.7**	**11.2**	71.9	17.3	68.2	15.48
CBVa	**86.7**	1×10^{-3}	80.0	2×10^{-3}	81.6	2.6×10^{-3}
MTR (s^{-1})	**98.4**	**0.003**	95.4	0.009	0	0.045
BAT (s)	**91.7**	**0.14**	90.0	0.18	89.1	0.19
T_1 (s)	98.6	**0.015**	**99.6**	0.016	98.0	0.029
Flip (rad)	**99.7**	0.029	98.6	**0.009**	84.7	0.062

Table 3: Correlation (in %) and RMSE (units in the parameter column) of each estimated parameter map with the corresponding ground truth map in the anthropomorphic digital phantom.
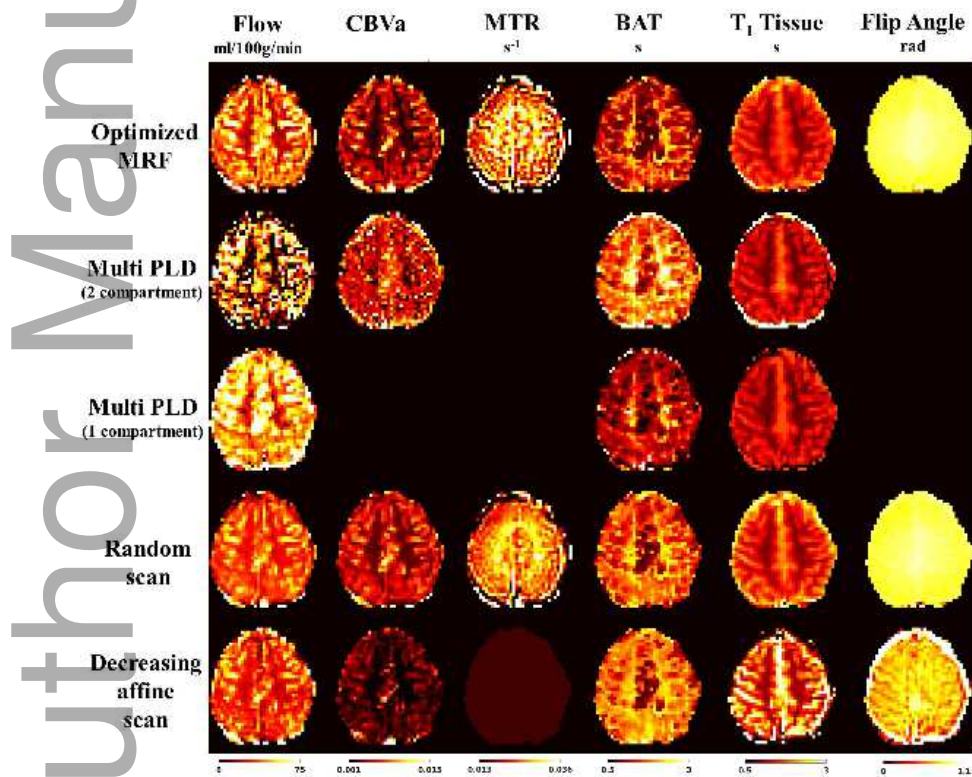
Figure 5: Comparison of the parameter estimates from various tested methods for a single subject. None of the methods used any spatial smoothing of the estimated maps or the ASL signal volume.

12

3.3 In vivo performance

It took approximately 1s to estimate each 64×64 parameter map for the MRF methods using the designated neural networks for the task on a 12GB NVIDIA Titan X Pascal GPU. The two stage fit for the multi-PLD data required approximately 1200s to estimate four 64×64 maps on a Intel Xeon E5-2650 with 40 cores. Fig. 5 compares the six estimated maps from a single human subject across all evaluated techniques. To gauge a sense of agreement between two-compartmental estimates from regression based ASL Fingerprinting and multi-PLD methods, Fig. 6 compares the mean gray matter CBF, BAT and CBVa across the six subjects, as well as the associated average T_1s for both gray and white matter using scatter plots. Fig. 7 shows a 'goodness-of-fit' comparison between the acquired signal and a 'synthetic' signal produced from the modeled equations (1)-(3) averaged over a region of interest. The synthetic signals were obtained by passing the parameters estimated from the neural networks through the ASL signal model.
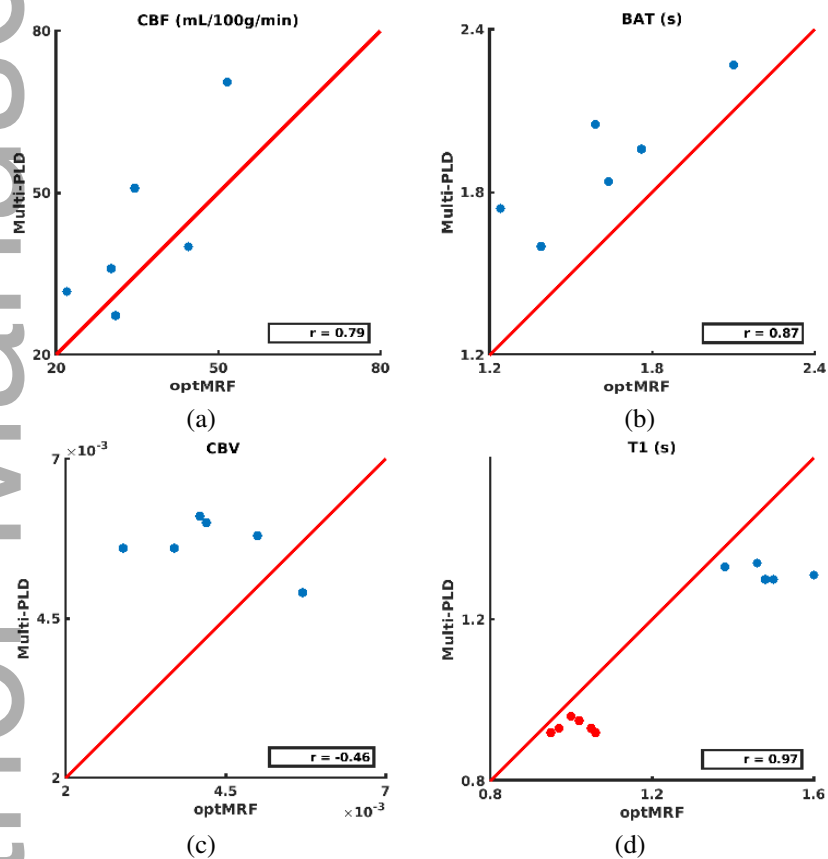
Figure 6: Scatter plots of slice-wide average estimates from optimized MRF vs multi-PLD of: (a) gray matter CBF, (b) gray matter BAT, (c) gray matter CBVa and (d) gray (blue dots) and white (red dots) matter T_1.

13

4 Discussion

This work established a CRLB based optimization method for labeling durations for improving the information within an MRF-ASL scan, as a means to get more precise estimates from it for a fixed scan time. This enables us to 'get the most' out of available scan time, and is of particular importance because of the trade-off between total scan time and precision of estimates, regardless of the estimator. Of course, it would be possible to reduce the scanning duration at the expense of overall precision. We adopted a neural network regression based estimation framework to avoid the granularity/imprecision of dictionary-search based estimators for problems with many parameters like ASL-MRF. The methods provided estimates for six parameters in both gray and white matter regions in the brain. We validated our methods in silico using a simulated anthropomorphic phantom, and in vivo against a multi-PLD method as well as two reference ASL-MRF scans. For easy comparison with 'state-of-the-art' MRF ASL, 'decreasing affine scan' was very similar to the Perlin schedule used in [35], but comparatively yielded lower predictions of normalized standard deviation, while 'random scan' was similar to the one used in [41]. In most cases, the CRLB predictions were reflected in the performance of various methods in a relative sense. The following subsections elaborate on our observations from section 3.

4.1 Optimized Scan Design

From the predicted standard deviations in Table 2, it is apparent that the optimized scan either at least performs comparably, or outperforms the other two at precisely estimating all relevant parameters. In particular, the overall cost function for the optimized labeling schedule is significantly lower than that for the others. This hints its potential for improved precision at jointly estimating all the modeled dependencies in the ASL signal. The MTR parameter contributes significantly to the overall variance of estimates, but incorporating it into our model may provide additional information about tissue health and reduce bias in estimates of perfusion. We also find that while a lot of variation in the labeling durations can help in the estimation of T_1 and Flip angles, it can be detrimental when attempting to estimate Perfusion (CBF), Blood Volume Fraction (CBVa) or Arterial Transit Times (BAT). Importantly, some of the predicted normalized standard deviations are very high even after optimization, but this is because the reported CRLBs are the average value over a very broad range of parameter combinations. Many of these yield little ASL signal under any acquisition scheme (consider a voxel with very low perfusion and long transit time); the method performs significantly better (normalized std. dev. of perfusion estimates decreases to 22.5% , while that of MTR is 13.6%) when evaluated over a smaller, more normative range. (This normative range was $\pm 2.5\%$ around ground truth perfusion 60 mL/100g/min, BAT 1.2s, CBVa 0.01, MTR $0.01 s^{-1}$ and T_1 1.4s)

4.2 Simulated Anthropomorphic Pathological Phantoms

Fig. 4 illustrates that there is good agreement between the estimated and the ground truth maps across all parameters. Additionally, our estimation is able to capture both the abnormally elevated and diminished regions of flow in the perfusion maps. This property is a consequence of: (i) optimizing the scan design over a large parameter range, (ii) training the neural network using a wide range of training parameters (Table 1).

Table 3 shows that for most estimated parameters, in comparison to the reference scans, our optimization leads to comparable or better correlation coefficients between truth and estimates. For perfusion in particular, we noted that the optimized scan yielded estimates that were significantly more aligned to the truth than the other scans. It was also intriguing to note that 'decreasing affine scan' regressed the same value of MTR ($\approx$ 0.015) for all inputs, thereby returning a correlation coefficient of 0%. Our conjecture is that this may be due

14

to the neural network being unable to learn from the training data due to the insensitivity of the fingerprints to MTR. We also observed that the correlation coefficent associated with perfusion for this specific scan was lower than the others, even though its predicted normalized standard deviation was comparable to that of the optimized scan. We therefore hypothesize that predictions of low normalized standard deviation may not always translate to high correlation between truth and estimates in the case of a biased estimator. This is because variable estimation bias at different points in the parameter space may lead to low correlation, despite the precision in estimates. For each estimated parameter, we calculated the RMSE with respect to ground truth, and found that the optimized MRF-ASL scan estimates report lower values of RMSE than those from the reference MRF-ASL scans in a majority of parameters. We also noticed that some of the estimates show a consistent bias with the ground truth. This is possibly due to the difference in the distribution of ground truth parameter values in training and testing data. The training data had a uniform random prior, but the test data has the distribution of an SPM12 phantom.

4.3 In vivo performance

Fig. 5 illustrates that the performance of our designed method is relatively consistent with the predictions from the Cramer-Rao Bound (see Table 2). The map corresponding to the magnetization transfer rate looks the noisiest, while parameters like T_1 or BAT look much cleaner. The distinction between gray and white matter regions is also apparent across all relevant maps, even without any spatial smoothing or SNR boosting methods.

The comparisons between the optimized and reference MRF scans were also in accordance with our expectations based on Table 3. As evident in the depicted subject, 'decreasing affine scan' fails to estimate the MTRs, and the estimated T_1 maps have unreasonably high values in gray matter. Moreover, even the flip angle map for this scan shows significant artefactual contrast between gray and white matter, which are absent in the other MRF methods. The maps yielded by 'random scan' show agreement with the optimized scan, but we observe that the MTR maps from the former are less informative, and exhibit more artifacts. These trends between the optimized and reference scans were noted to be consistent across all four subjects studied.

Fig. 5, shows that the MRF methods are able to estimate CBF, BAT and CBVa values in white matter, while the two-compartment multi-PLD method fails to do so: instead, the corresponding maps show many near-zero perfusion voxels in white matter regions, along with abnormally high transit times. The coefficient of variation (std. deviation/mean) for white matter perfusion averaged across all six subjects was 1.19 for the multi-PLD method, compared to 0.16 for optimized MRF-ASL. In gray matter, the avg. coefficient of variation was 0.54 for multi-PLD and 0.27 for optimized MRF-ASL. The obtained CBVa map from the latter method also appears extremely noisy, and is unable to pick out vasculature in the slice as effectively. We hypothesize that the poor performance in the multi-PLD method was due to the fact that its acquisition parameters were optimized for a single compartment model that does not account for CBVa. We also noticed that the single compartment estimates reported higher values perfusion and lower BATs than two-compartment estimates. This is an expected observation due to the label present in the arteries seeping into the acquired tissue signal under the single compartment assumption, considering that no arterial suppression was used in our acquisition and the post-labeling delays weren't very long [1].

In Fig. 6 (a)-(b), we found the estimates from optimized MRF-ASL and multi-PLD to be fairly consistent, as observed from the high correlation coefficients between the two methods, for measurements of CBF as well as BAT. However, we note that the multi-PLD method consistently reports higher BATs in gray matter with a two-compartment fit. Fig. 6 (c) shows a similar scatter plot for CBVa, but there is little agreement between the methods. This may be due to the fact that the estimates of CBVa from the multi-PLD method

15

have a lot of variance across the brain, for reasons explained above. The T_1 estimates for the two methods are compared in Fig. 6 (d), with the red dots indicating white matter T_1s, and the blue ones indicating gray matter T_1s. We see that while the optimized MRF method generally yields higher values of T_1, the measurements agree well.
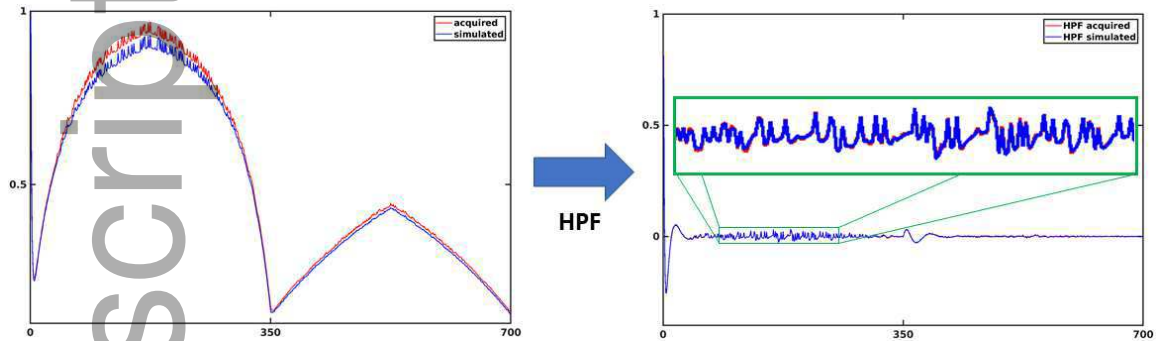

Figure 7: ROI-averaged comparison of acquired signals and simulated signals which were generated from our model, based on neural network estimates. The left and right panes show the signals before and after high pass filtering, respectively.

Fig. 7 reinforces that high pass filtering the fingerprint signals significantly improves the signal fidelity in the small, high frequency components, that correspond to manifestations of hemodynamic phenomenon. This increased agreement is because using a high pass filter removes low frequency components related to receiver drift, etc. that introduces discrepancies that were not accounted for in the model.

5 Conclusion

We have developed a framework for optimizing the scan design for MRF-ASL that yields more precise estimates in gray and white matter, than other scan designs for MRF-ASL used in literature, and has a lower coefficent of variation in white matter and gray matter perfusion than a reference multi-PLD method, while mainitaining agreement in gray matter perfusion and transit times. We also introduced a neural network regressor for fast precise estimates from ASL fingerprints. Combined with scan optimization, the neural networks can estimate six parameters from a single 600s ASL scan in a very short processing time and bypass quantization errors. While the work presented here is intended to serve as proof of concept, our comparisons with reference scans show that we are able to significantly improve upon the precision of the state-of-the-art in MR Fingerprinting ASL. Future work will focus on adapting the present scheme for 3D acquisition, including background suppression pulses and reducing the scan duration to make the technique practical in the clinical setting.

6 Acknowledgements

16

References

[1] D. C. Alsop and J. A. Detre. Reduced Transit-Time Sensitivity in Noninvasive Magnetic Resonance Imaging of Human Cerebral Blood Flow. *Journal of Cerebral Blood Flow & Metabolism*, 16(6):1236–1249, 11 1996.

[2] D.S. Bolar, D.L. Levin, S.R. Hopkins, L.F. Frank, T.T. Liu, E.C. Wong, and R.B. Buxton. Quantification of regional pulmonary blood flow using ASL-FAIRER. *Magnetic Resonance in Medicine*, 55(6):1308–1317, 6 2006.

[3] J L Boxerman, K M Schmainda, R M Weisskoff, L.R. Schultz, J.P. Rock, J. Gutierrez, S.C. Patel, J. Ewing, and T. Mikkelsen. Relative cerebral blood volume maps corrected for contrast agent extravasation significantly correlate with glioma tumor grade, whereas uncorrected maps do not. *AJNR. American journal of neuroradiology*, 27(4):859–67, 4 2006.

[4] M. J. Brookes, P. G. Morris, P. a. Gowland, and S. T. Francis. Noninvasive measurement of arterial cerebral blood volume using Look-Locker EPI and arterial spin labeling. *Magnetic Resonance in Medicine*, 58(1):41–54, 2007.

[5] R B Buxton, L R Frank, E C Wong, B Siewert, S Warach, and R R Edelman. A general kinetic model for quantitative perfusion imaging with arterial spin labeling. *Magnetic resonance in medicine : official journal of the Society of Magnetic Resonance in Medicine / Society of Magnetic Resonance in Medicine*, 40:383–396, 1998.

[6] Thibaut Capron, Thomas Troalen, Patrick J. Cozzone, Monique Bernard, and Frank Kober. Cine-ASL: A steady-pulsed arterial spin labeling method for myocardial perfusion mapping in mice. Part II. Theoretical model and sensitivity optimization. *Magnetic Resonance in Medicine*, 70(5):1399–1408, 2013.

[7] Yufen Chen, Danny J.J. Wang, and John A. Detre. Test-retest reliability of arterial spin labeling with common labeling strategies. *Journal of Magnetic Resonance Imaging*, 33(4):940–949, 4 2011.

[8] Ouri Cohen, Bo Zhu, and Matthew S. Rosen. MR fingerprinting Deep RecOnstruction NEtwork (DRONE). *Magnetic Resonance in Medicine*, 80(3):885–894, 9 2018.

[9] Cedric De Bazelaire, Neil M Rofsky, Guillaume Duhamel, M Dror Michaelson, Daniel George, and David C Alsop. Arterial spin labeling blood flow magnetic resonance imaging for the characterization of metastatic renal cell carcinoma(1). *Academic radiology*, 12(3):347–57, 3 2005.

[10] A R Deibler, J M Pollock, R A Kraft, H Tan, J H Burdette, and J A Maldjian. Arterial spin-labeling in routine clinical practice, part 1: technique and artifacts. *AJNR. American journal of neuroradiology*, 29(7):1228–34, 8 2008.

[11] John A. Detre, John S. Leigh, Donald S. Williams, and Alan P. Koretsky. Perfusion imaging. *Magnetic Resonance in Medicine*, 23(1):37–45, 1 1992.

[12] John A. Detre, Hengyi Rao, Danny J.J. Wang, Yu Fen Chen, and Ze Wang. Applications of arterial spin labeled MRI in the brain. *Journal of Magnetic Resonance Imaging*, 35(5):1026–1037, 5 2012.

[13] K. J. (Karl J.) Friston, John Ashburner, Stefan Kiebel, Thomas Nichols, and William D. Penny. *Statistical parametric mapping : the analysis of funtional brain images*. Elsevier/Academic Press, 2007.

[14] Robert A. Gatenby, Olya Grove, and Robert J. Gillies. Quantitative Imaging in Cancer Evolution and Ecology. *Radiology*, 269(1):8–14, 10 2013.

[15] G A R Y H Glover, T I E Iang L I, and D Avid R Ess. Image-Based Method for Retrospective Correction of Physiological Motion Effects in fMRI : RETROICOR. 167(March):162–167, 2000.

[16] Sven Haller, Greg Zaharchuk, David L. Thomas, Karl-Olof Lovblad, Frederik Barkhof, and Xavier Golay. Arterial Spin Labeling Perfusion of the Brain: Emerging Clinical Applications. *Radiology*, 281(2):337–356, 11 2016.

[17] V B Ho, J G Smirniotopoulos, F M Murphy, E J Rushing, K. Yamashita, E. Nagao, T. Shono, M. Mizoguchi, S. Nagata, T. Sasaki, S.O. Suzuki, T. Iwaki, K. Kobayashi, F. Mihara, and H. Honda. Radiologic-pathologic correlation: hemangioblastoma. *AJNR. American journal of neuroradiology*, 13(5):1343–52, 4 2008.

[18] Diederik P. Kingma and Jimmy Ba. Adam: A Method for Stochastic Optimization. 12 2014.

[19] John Kucharczyk, Jan Mintorovitch, Haleh S. Asgari, and Michael Moseley. Diffusion/perfusion MR imaging of acute cerebral ischemia. *Magnetic Resonance in Medicine*, 19(2):311–315, 6 1991.

[20] Anish Lahiri, Jeffrey A. Fessler, and Luis Hernandez-Garcia. Optimized Scan Design for ASL Fingerprinting and Multiparametric Estimation using Neural Network Regression. In *Proceedings of the 26th Annual Meeting of International Society for Magnetic Resonance in Medicine (ISMRM)*, page 309, 2018.

[21] Seung Soo Lee, Jae Ho Byun, Beom Jin Park, Seong Ho Park, Namkug Kim, Bumwoo Park, Jeong Kon Kim, and Moon-Gyu Lee. Quantitative analysis of diffusion-weighted magnetic resonance imaging of the pancreas: Usefulness in characterizing solid pancreatic masses. *Journal of Magnetic Resonance Imaging*, 28(4):928–936, 10 2008.

[22] Thomas T. Liu and Eric C. Wong. A signal processing model for arterial spin labeling functional MRI. *NeuroImage*, 24(1):207–215, 1 2005.

[23] Torben E. Lund, Kristoffer H. Madsen, Karam Sidaros, Wen-Lin Luo, and Thomas E. Nichols. Non-white noise in fMRI: Does modelling have an impact? *NeuroImage*, 29(1):54–66, 1 2006.

[24] Dan Ma, Vikas Gulani, Nicole Seiberlich, Kecheng Liu, Jeffrey L. Sunshine, Jeffrey L. Duerk, and Mark A. Griswold. Magnetic resonance fingerprinting. *Nature*, 495(7440):187–192, 3 2013.

[25] Jeanette A. Mumford, Luis Hernandez-Garcia, Gregory R. Lee, and Thomas E. Nichols. Estimation efficiency and statistical power in arterial spin labeling fMRI. *NeuroImage*, 33(1):103–114, 10 2006.

[26] Gopal Nataraj, Jon Fredrick Nielsen, and Jeffrey A. Fessler. Optimizing MR Scan Design for Model-Based T1, T2 Estimation from Steady-State Sequences. *IEEE Transactions on Medical Imaging*, PP(99):467–477, 2016.

[27] Gopal Nataraj, Jon-Fredrik Nielsen, Clayton Scott, and Jeffrey A. Fessler. Dictionary-Free MRI PERK: Parameter Estimation via Regression with Kernels. *IEEE Transactions on Medical Imaging*, 37(9):2103–2114, 9 2018.

18

[28] Tomoyuki Noguchi, Takashi Yoshiura, Akio Hiwatashi, Osamu Togao, Koji Yamashita, Eiki Nagao, and Hiroshi Honda. Arterial spin-labelin magnetic resonance imaging: The timing of regional maximal perfusion-related signal intensity revealed by a multiphase technique. *Japanese Journal of Radiology*, 30(2):137–145, 2 2012.

[29] Laura M. Parkes. Quantification of cerebral perfusion using arterial spin labeling: Two-compartment models. *Journal of Magnetic Resonance Imaging*, 22(6):732–736, 2005.

[30] Joanna E. Perthen, Mark Bydder, Khaled Restom, and Thomas T. Liu. SNR and functional sensitivity of BOLD and perfusion-based fMRI using arterial spin labeling with spiral SENSE at 3 T. *Magnetic Resonance Imaging*, 26(4):513–522, 5 2008.

[31] Anita Ramani, Jens H. Jensen, and Joseph A. Helpern. Quantitative MR Imaging in Alzheimer Disease. *Radiology*, 241(1):26–44, 10 2006.

[32] Giles Roditi, Jeffrey H. Maki, George Oliveira, and Henrik J. Michaely. Renovascular imaging in the NSF Era. *Journal of Magnetic Resonance Imaging*, 30(6):1323–1334, 12 2009.

[33] D I Rosenthal, N W Barton, K A McKusick, B R Rosen, S C Hill, F P Castronovo, R O Brady, S H Doppelt, and H J Mankin. Quantitative imaging of Gaucher disease. *Radiology*, 185(3):841–5, 12 1992.

[34] Pan Su, Deng Mao, Peiying Liu, Yang Li, Marco C. Pinho, Babu G. Welch, and Hanzhang Lu. Multiparametric estimation of brain hemodynamics with MR fingerprinting ASL. *Magnetic Resonance in Medicine*, 00(November):1–12, 2016.

[35] Pan Su, Deng Mao, Peiying Liu, Yang Li, Marco C Pinho, Babu G Welch, and Hanzhang Lu. Multiparametric Estimation of Brain Hemodynamics With MR Fingerprinting ASL. *Magn Reson Med*, 78:1812–1823, 2017.

[36] P. van Gelderen, J.A. de Zwart, and J.H. Duyn. Pittfalls of MRI measurement of white matter perfusion based on arterial spin labeling. *Magnetic Resonance in Medicine*, 59(4):788–795, 4 2008.

[37] Yingbing Wang, Tarik K. Alkasab, Ozden Narin, Rosalynn M. Nazarian, Rathachai Kaewlai, Jonathan Kay, and Hani H. Abujudeh. Incidence of Nephrogenic Systemic Fibrosis after Adoption of Restrictive Gadolinium-based Contrast Agent Guidelines. *Radiology*, 260(1):105–111, 7 2011.

[38] Jonathan M. Watts, Christopher T. Whitlow, and Joseph A. Maldjian. Clinical applications of arterial spin labeling. *NMR in Biomedicine*, 26(8):892–900, 8 2013.

[39] Eric C. Wong, Richard B. Buxton, and Lawrence R. Frank. A theoretical and experimental comparison of continuous and pulsed arterial spin labeling techniques for quantitative perfusion imaging. *Magnetic Resonance in Medicine*, 40(3):348–355, 9 1998.

[40] Joseph G. Woods, Michael A. Chappell, and Thomas W. Okell. A general framework for optimizing arterial spin labeling MRI experiments. *Magnetic Resonance in Medicine*, 81(4):2474–2488, 4 2019.

[41] Katherine L. Wright, Yun Jiang, Dan Ma, Douglas C. Noll, Mark A. Griswold, Vikas Gulani, and Luis Hernandez-Garcia. Estimation of perfusion properties with MR Fingerprinting Arterial Spin Labeling. *Magnetic Resonance Imaging*, 50:68–77, 7 2018.

19

[42] Jingyi Xie, Daniel Gallichan, Roger N. Gunn, and Peter Jezzard. Optimal design of pulsed arterial spin labeling MRI experiments. *Magnetic Resonance in Medicine*, 59(4):826–834, 2008.

[43] Bo Zhao, Justin P. Haldar, Congyu Liao, Dan Ma, Mark A. Griswold, Kawin Setsompop, and Lawrence L. Wald. Optimal Experiment Design for Magnetic Resonance Fingerprinting: Cram\'er-Rao Bound Meets Spin Dynamics. (Ml):1–15, 2017.

[44] Jinyuan Zhou, David A. Wilson, John A. Ulatowski, Richard J. Traystman, and Peter C. M. van Zijl. Two-Compartment Exchange Model for Perfusion Quantification Using Arterial Spin Tagging. *Journal of Cerebral Blood Flow & Metabolism*, 21(4):440–455, 2001.

20
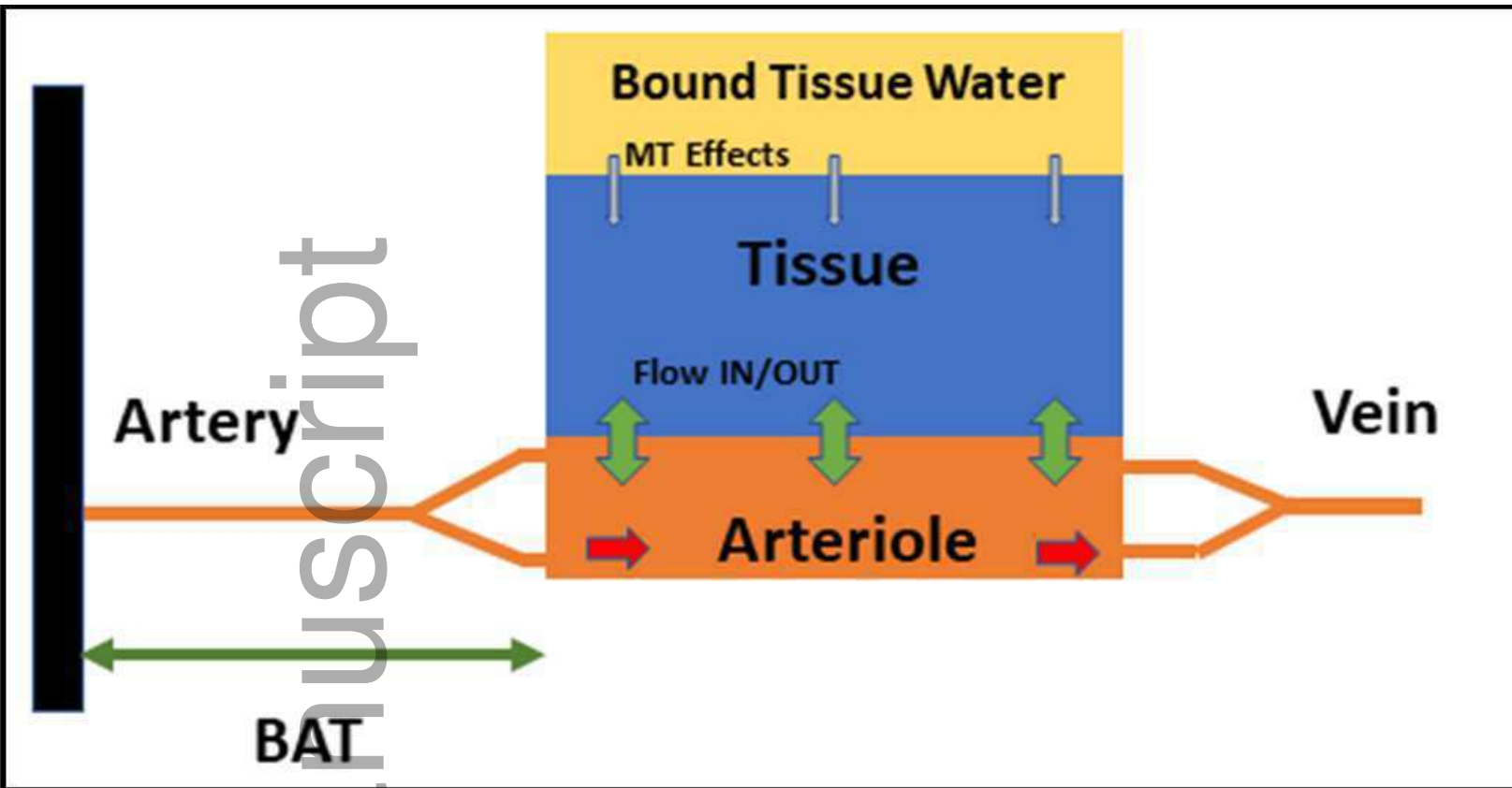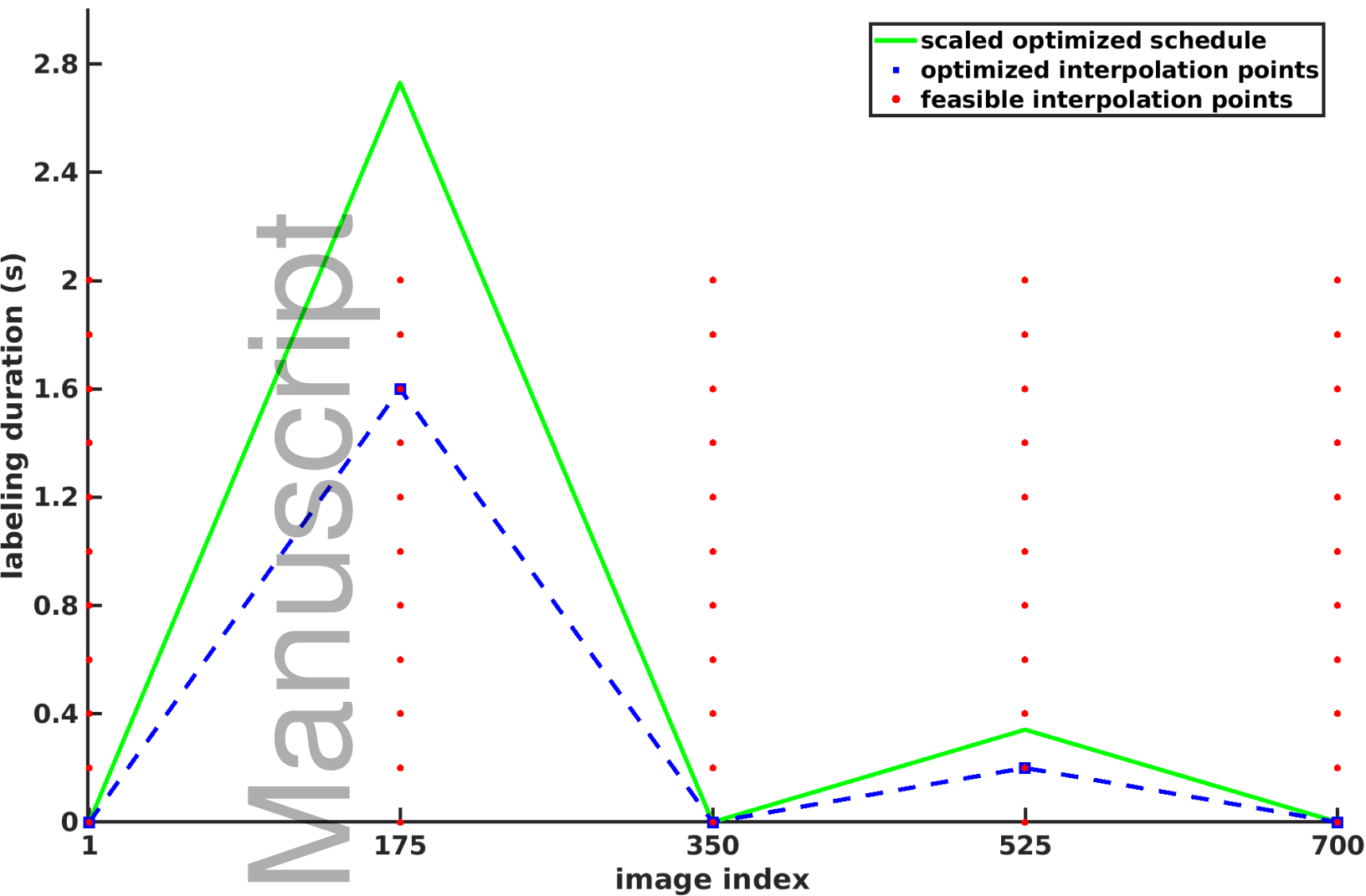
mrm_28051_f1.eps

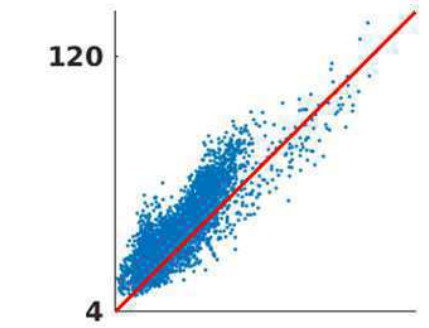mrm_28051_f2.eps

Stage: Training
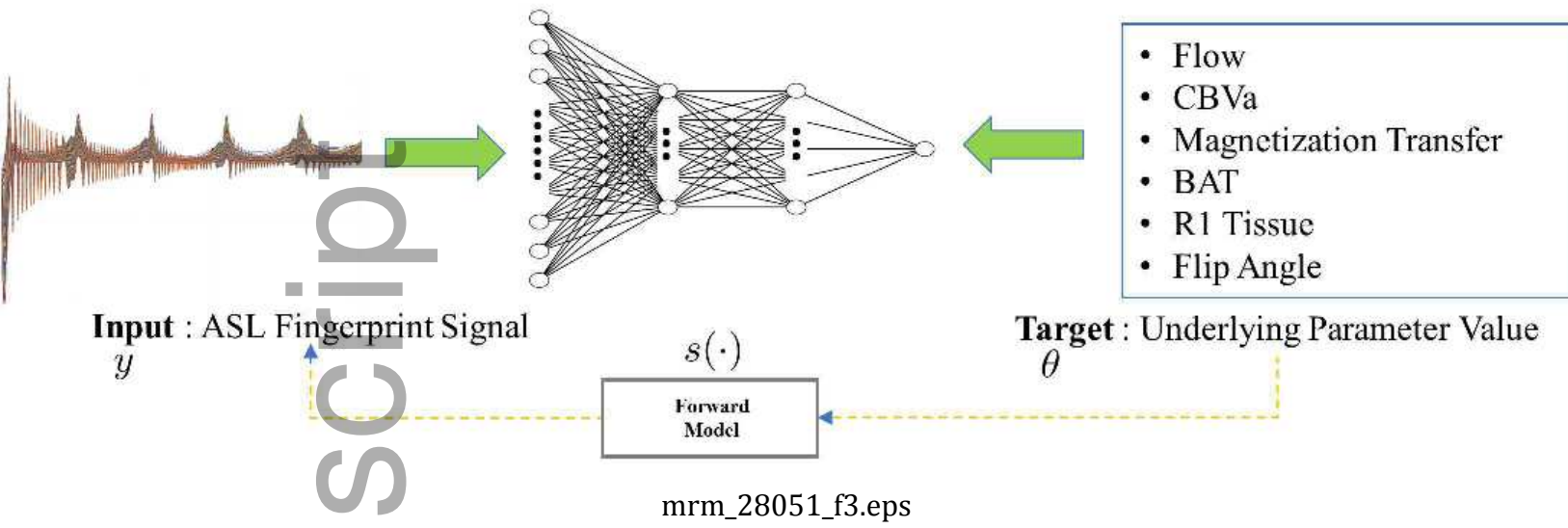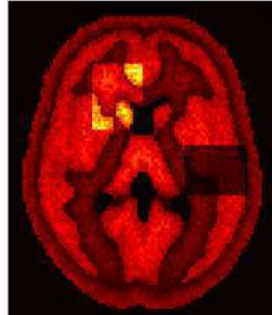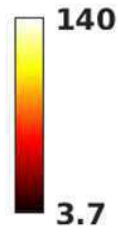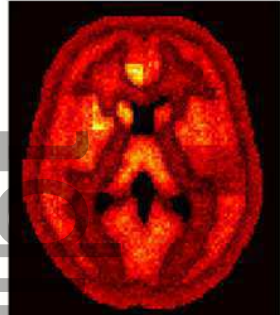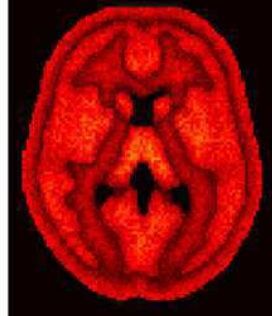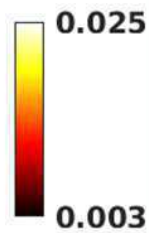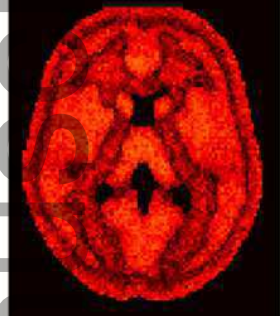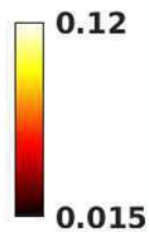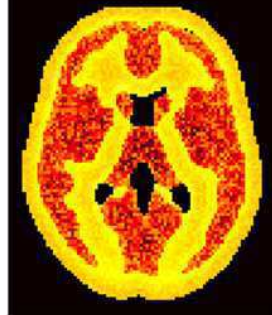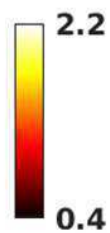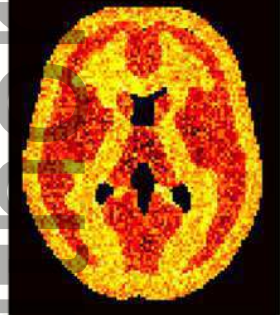
Input : ASL Fingerprint Signal
y

- Flow
- CBVa
- Magnetization Transfer
- BAT
- R1 Tissue
- Flip Angle

Target : Underlying Parameter Value
θ

$s(\cdot)$

Forward
Model

mrm_28051_f3.eps

	Flow ml/100g/min	CBVa	MTR s⁻¹	BAT s	T₁ Tissue s	Flip Angle rad

Column headers: **Flow** ml/100g/min, **CBVa**, **MTR** s^{-1}, **BAT** s, **T$_1$ Tissue** s, **Flip Angle** rad

Row labels:
- **Optimized MRF**
- **Multi PLD (2 compartment)**
- **Multi PLD (1 compartment)**
- **Random scan**
- **Decreasing affine scan**

Colorbar ranges:
- 6 — 75
- 0.001 — 0.015
- 0.013 — 0.036
- 0.5 — 3
- 0.5 — 3
- 0 — 1.1

mrm_28051_f5.eps

CBF (mL/100g/min)

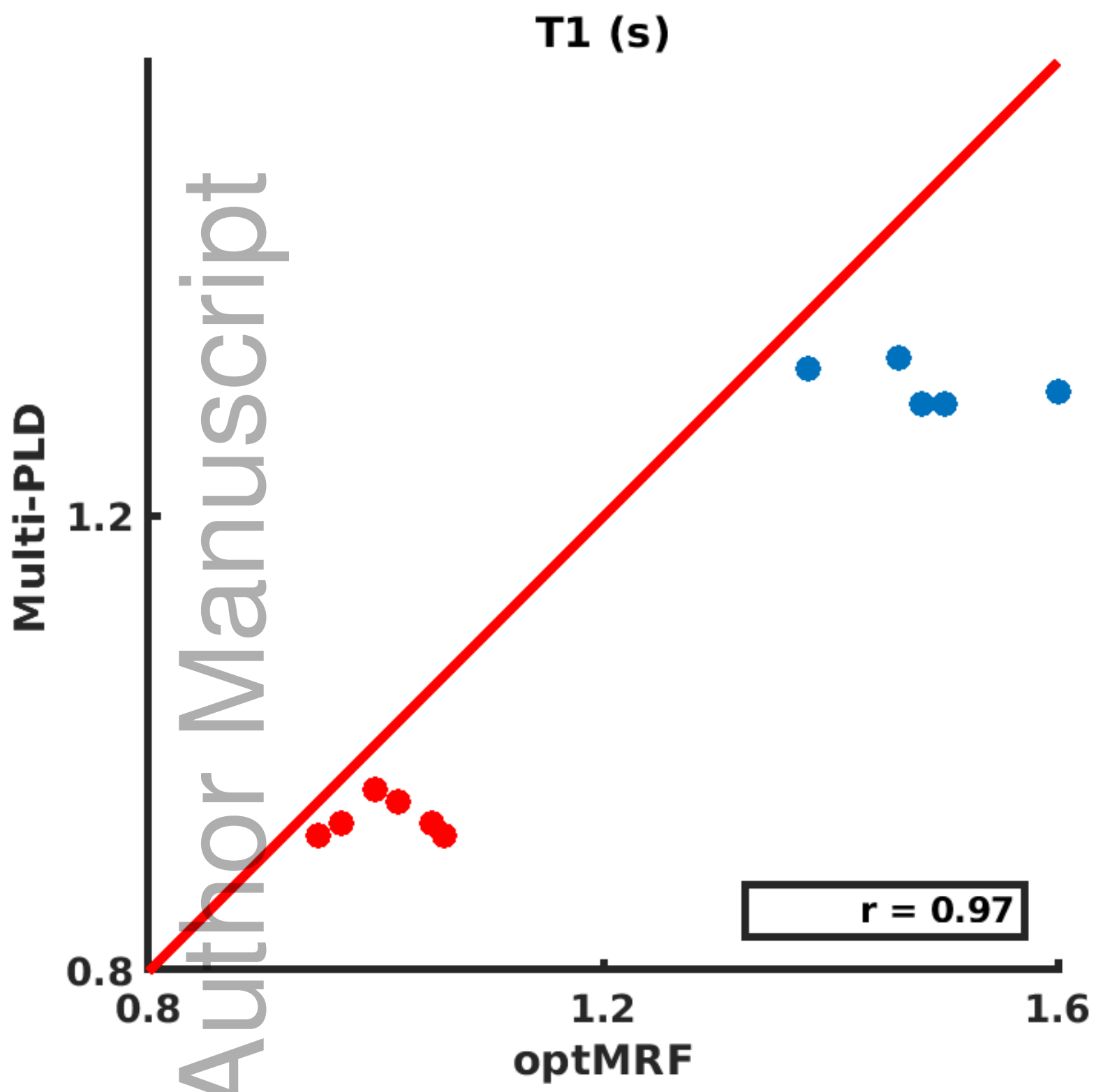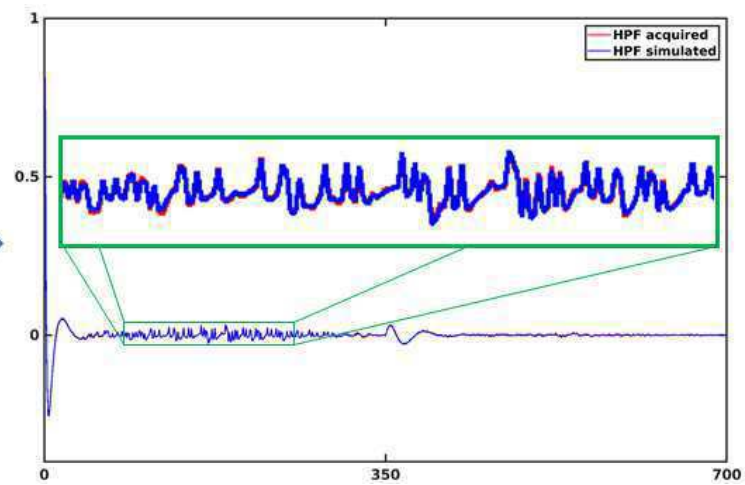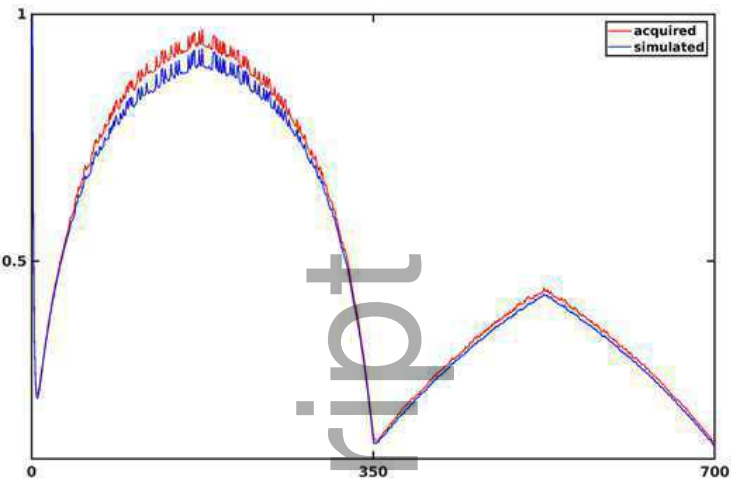
r = 0.79

mrm_28051_f6a.eps

BAT (s)

mrm_28051_f6b.eps

CBV

mrm_28051_f6c.eps

T1 (s)
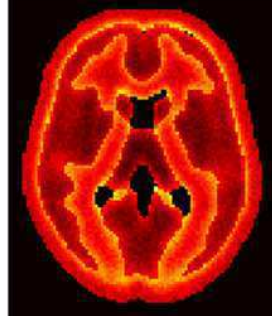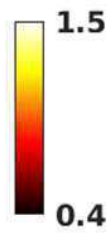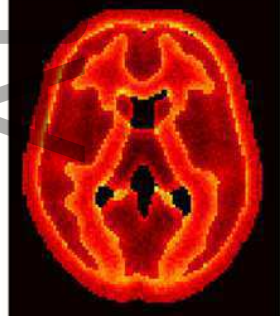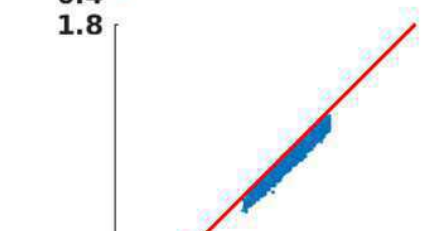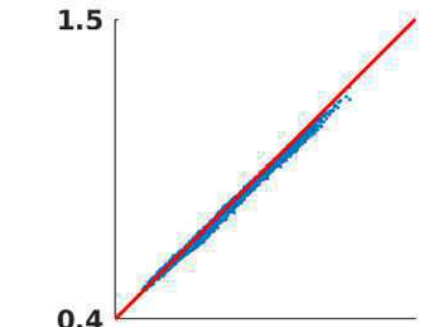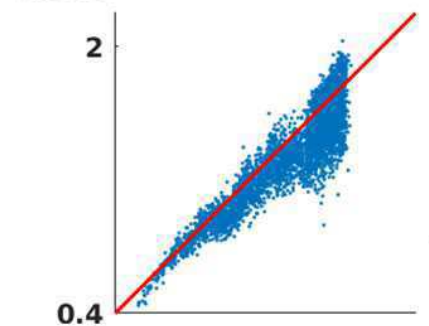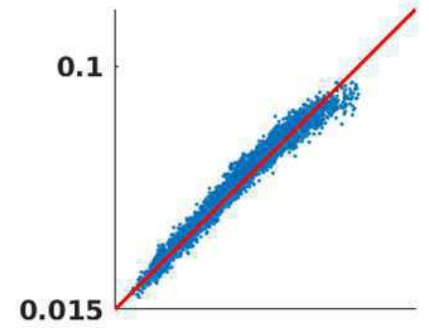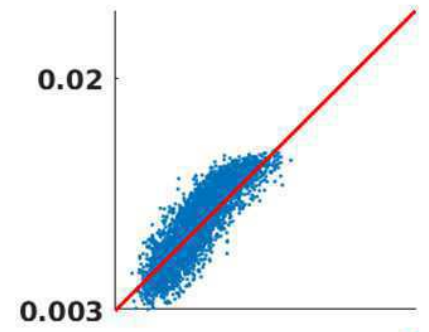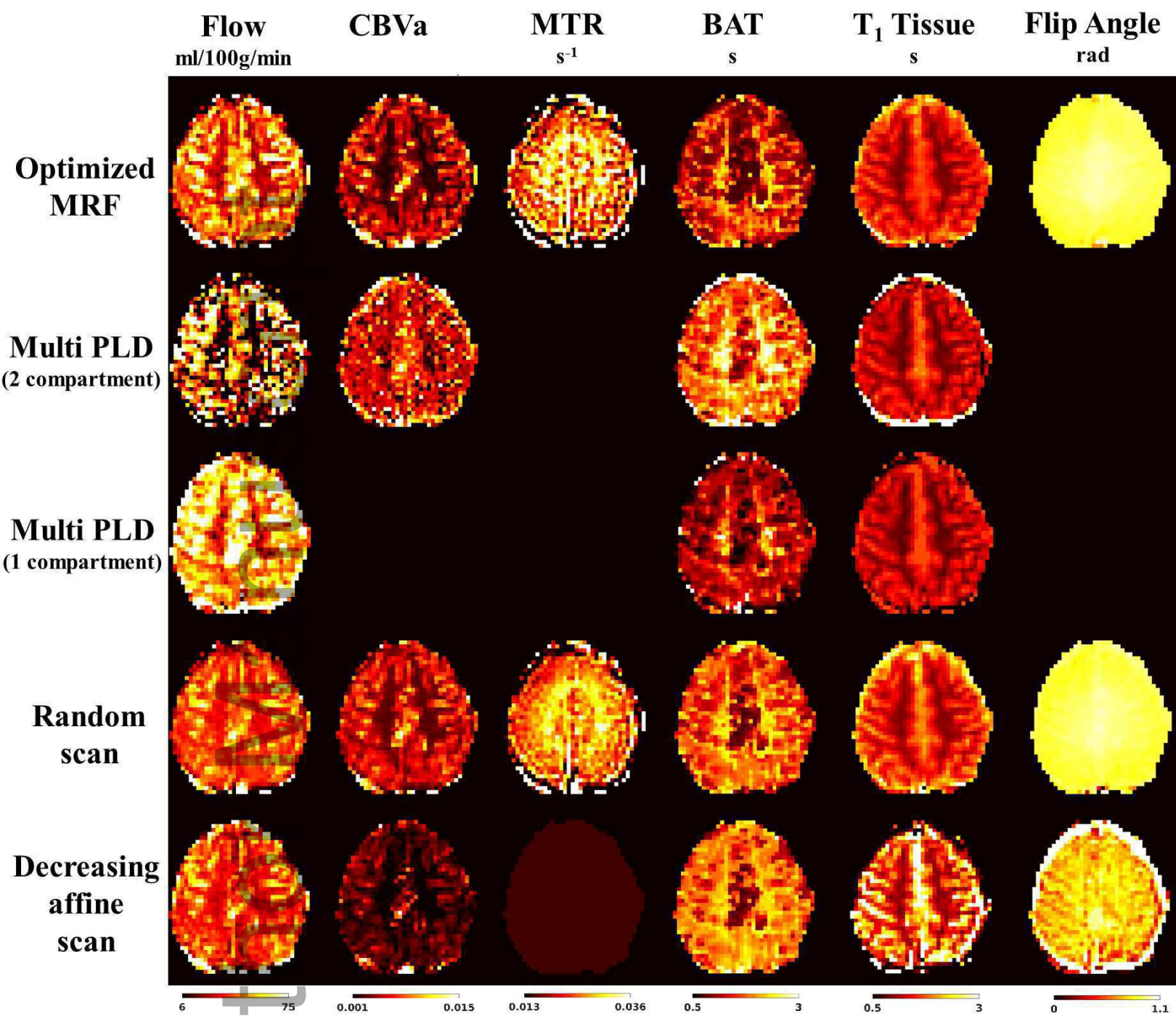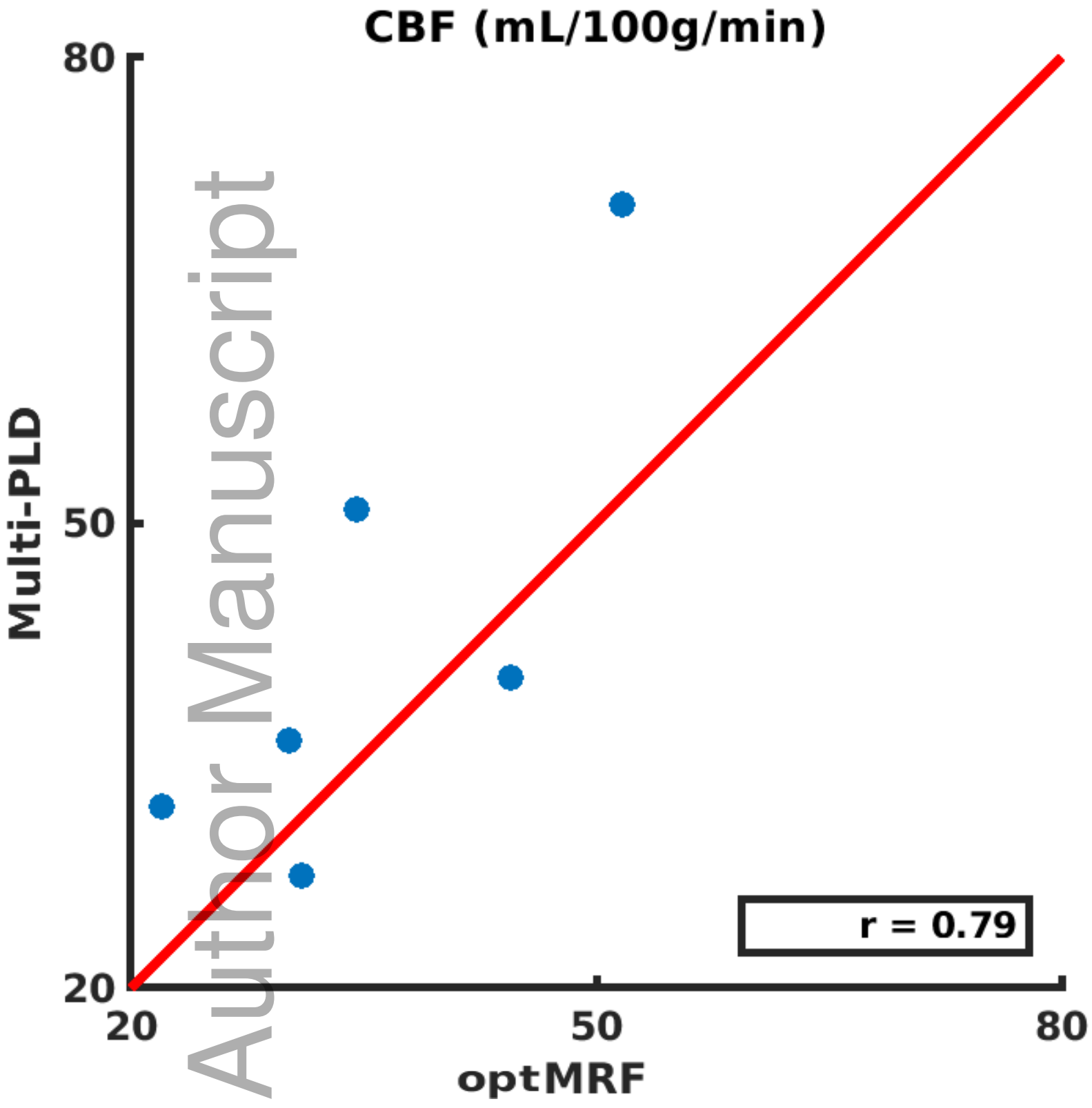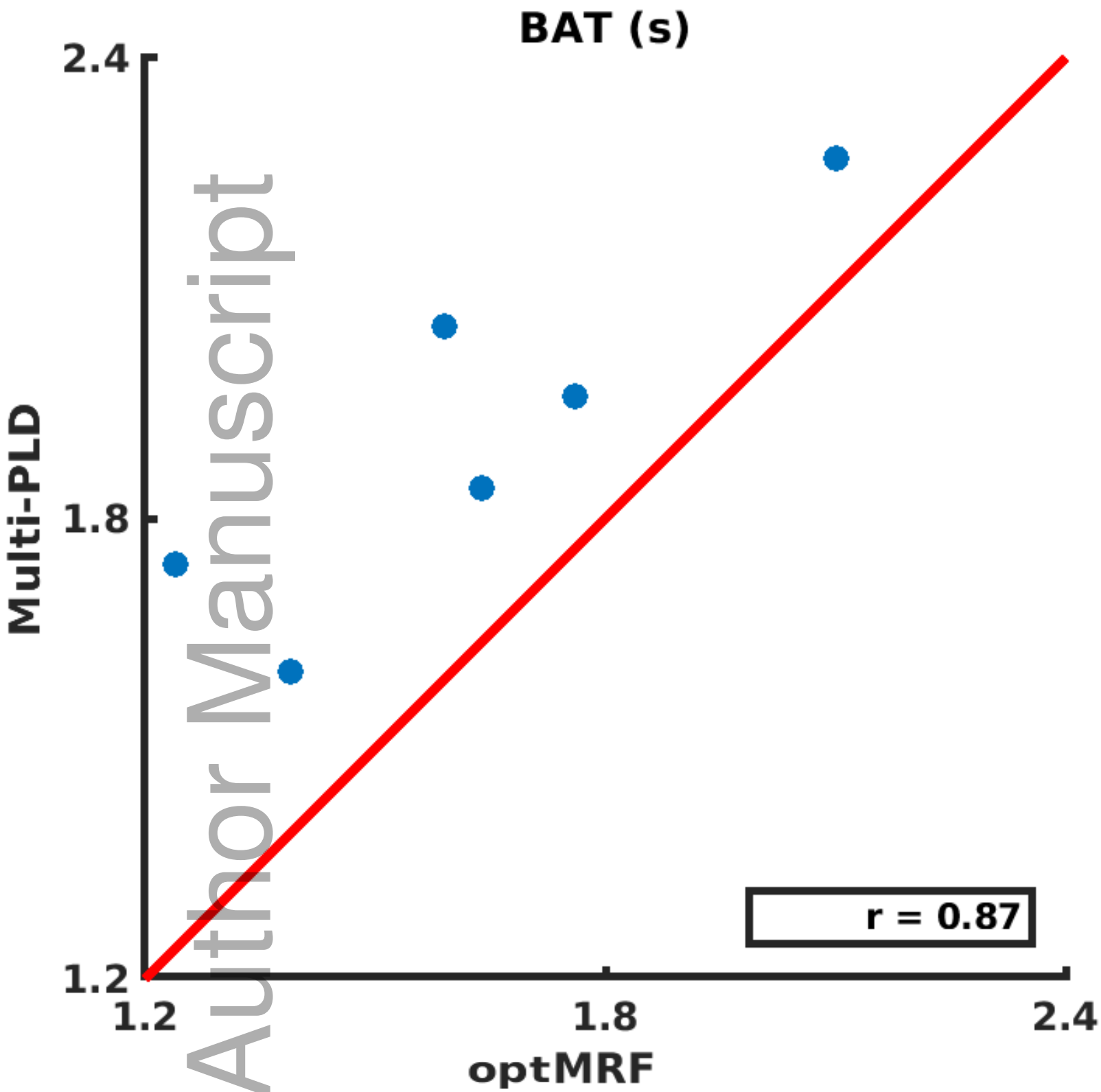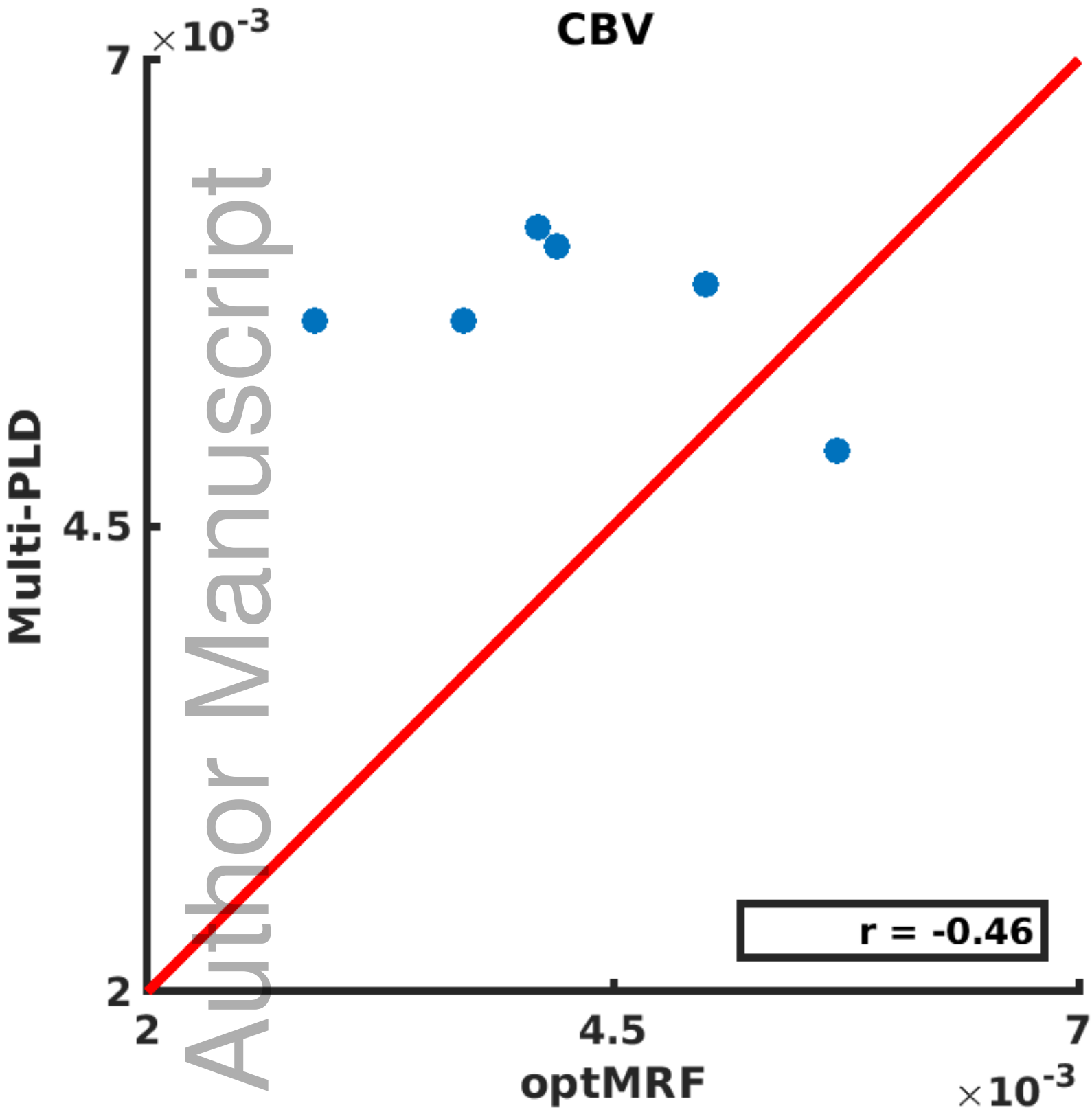
mrm_28051_f6d.eps

mrm_28051_f7.eps